1 **Future permafrost degradation under climate change in a headwater catchment of Central**

2 **Siberia: quantitative assessment with a mechanistic modelling approach**

3 Thibault Xavier[1], Laurent Orgogozo[1*], Anatoly S. Prokushkin[2], Esteban Alonso-González[3], Simon

4 Gascoin[4], Oleg S. Pokrovsky[1,5]

5 [1]Geoscience Environnement Toulouse (GET), CNRS, UMR5563, Toulouse, 31400, France
6 [2]V.N. Sukachev Institute of Forest SB RAS, Russia
7 [3]Instituto Pirenaico de Ecología, Consejo Superior de Investigaciones Científicas (IPE-CSIC), Jaca,
8 Spain
9 [4]Centre d'Etudes Spatiales de la Biosphère, Université de Toulouse, CNRS/CNES/IRD/INRA/UPS,
10 Toulouse, France
11 [5]BIO-GEO-CLIM Laboratory, Tomsk State University, Tomsk, Russia

12 * *Corresponding author*: Laurent Orgogozo (laurent.orgogozo@get.omp.eu)

13 **Abstract**

14 Permafrost thawing as a result of climate change has major consequences locally and globally for

15 the biosphere as well as for human activities. The quantification of its extent and dynamics under

16 different climate scenarios is needed to design local adaptation and mitigation measures and to

17 better understand permafrost climate feedbacks. To this end, numerical simulation can be used to

18 explore the response of soil thermo-hydric regimes to changes in climatic conditions. Mechanistic

19 approaches minimize modelling assumptions by relying on the numerical resolution of continuum

20 mechanics equations, but involve significant computational effort. In this work, the permaFoam

21 solver is used along with high-performance computing resources to assess the impact of four

22 climate scenarios of the Coupled Model Intercomparison Project - Phase 6 (CMIP6) on permafrost

23 dynamics within a pristine, forest-dominated watershed in the continuous permafrost zone. Using

24 these century time-scale simulations, changes in soil temperature, soil moisture, active layer

25 thickness and water fluxes are quantified, assuming no change in vegetation cover. The most severe

26 scenario (SSP5-8.5) suggests a dramatic increase in both active layer thickness and annual

27 evapotranspiration, with maximum values on the watershed reached in 2100 of +46% and +29%

28 respectively. For the active layer thickness, in current climatic conditions it would correspond to a

29 560 km southward shift. Moreover, in this scenario thermal equilibrium of near-surface permafrost

30 with the new climatic conditions would not be reached in 2100, suggesting a further thawing of

31 permafrost even in case of halting the climate change.

32 **Keywords**

33 Permafrost, climate change, boreal forest, numerical modelling, high performance computing, soil

34 temperature, soil moisture, evapotranspiration.

1 Introduction

Permafrost is mostly situated in regions that are experiencing especially intense climate change, resulting in widespread warming and thawing with shrinking of its lateral extension and thickening of soil active layer (Biskaborn et al., 2019, Hu et al., 2022, Li et al., 2022a, 2022b). Permafrost thawing induces sizable changes in the environments (Walvoord and Kurylyk, 2016, Nitze et al., 2018, Makarieva et al., 2019, Jin et al., 2022, Wright et al., 2022) and for human activities (Shiklomanov et al., 2017, Strelestkiy et al., 2019, 2023, Hjort et al., 2018, 2022) in the Arctics and the sub-Arctics. For instance, permafrost-thaw related decrease of soil moisture leads to an increase in boreal fire frequency (Kurylyk, 2019, Kim et al., 2020), while soil mechanical instabilities induced by permafrost thawing threaten population settlements (Ramage et al., 2021) and infrastructures (Bartsch et al., 2021). Moreover, permafrost thaw may exert significant controls on biogeochemical cycles of carbon and related metals (Sonke et al., 2018, Karlsson et al., 2021, Walvoord and Striegl, 2021) and climate dynamics (Miner et al., 2022, Park and Kug, 2022, de Vrese et al., 2023), with potentially major feedback on climate warming. Thus anticipating the evolution of permafrost cover and dynamics is of primary importance for understanding and mitigating the climate change induced impacts at high latitudes. For this, robust and accurate numerical simulations are required (Schneider von Deimling et al., 2022, Hu et al., 2023b).

Boreal forest is one of the largest biome on Earth (Gauthier et al., 2015), and 80% of its area is located in permafrost regions (Stuenzi et al., 2021). Given that most permafrost areas are covered by boreal forest. Due to the complexity of the biophysical processes involved, quantifying permafrost dynamics evolution in boreal forests under climate change requires mechanistic, high-resolution modelling approaches (Orgogozo et al., 2019). Meanwhile, the large extent of the considered areas makes the use of such approaches impracticable at global, continental or regional scale. As a consequence, mechanistic modelling of permafrost dynamics has to focus on processes at the watershed scale in headwater catchments with long term environmental monitoring, following a general trend in Arctic sciences (Speetjens et al., 2023, Vonk et al., 2023). In Arctic environments, the vegetation strongly controls surface energy budget (Fedorov et al., 2019, Oehri et al., 2022), interacts with climate dynamics (Park et al., 2020, Kyrdyanov et al., 2024) and drives water fluxes (Orgogozo et al., 2019). As such, vegetation should be taken into account when simulating the impact of climate warming on permafrost in boreal forest areas (Loranty et al., 2018, Kirdyanov et al., 2020, Holloway et al., 2020).

66 Quantitative mechanistic modeling of permafrost dynamics under climate change at the headwater
67 catchment scale requires large computational resources, because fine spatio-temporal discretisations
68 are needed due to the strong non-linearities and couplings of the involved physics (Kurylyk and
69 Watanabe, 2013). This is especially important for century long simulation periods (O'Neill et al.,
70 2016) and simulation domains with surfaces up to tens of square kilometers (e.g.: Arndal and Torp-
71 Jørgensen, 2020). Therefore, high performance computing techniques are needed (Orgogozo et al.,
72 2023).

73   In this study, we focus on a permafrost-dominated, forested watershed of central Siberia
74 which was subjected to long term environmental monitoring, the Kulingdakan watershed (e.g.:
75 Prokushkin et al., 2007, Mashukov et al., 2021). The objective is to assess the future state of
76 permafrost and ground thermal regime in this continuous permafrost, boreal forest environment
77 under different climate change scenarios at the century time scale. The permafrost status of this
78 catchment under current climatic conditions has already been investigated (Orgogozo et al., 2019).
79 Here, we simulate, using a mechanistic modelling approach, the permafrost dynamics at the
80 catchment scale until 2100 under various scenarios of climate change. The vegetation controls on
81 permafrost dynamics are partly included in the mechanistic modelling framework, considering
82 evapotranspiration fluxes (Orgogozo et al., 2019), and partly handled empirically, via the
83 accounting on the insulating effect of ground floor vegetation (Blok et al., 2011, Cazaurang et al.,
84 2023). However, because no changes of vegetation is explicitly considered, we assume constant
85 biomass and primary production and therefore investigate only the physical part of the response of
86 permafrost to climate change. We use the permaFoam High Performance Computing
87 cryohydrogeological simulator (Orgogozo et al., 2023) with a national level supercomputing
88 infrastructure, the Joliot-Curie supercomputer of the Très Grand Centre de Calcul (TGCC) of the
89 French Alternative Energies and Atomic Energy Commission (CEA). The simulated permafrost
90 thawing features in Kulingdakan are discussed and compared for the different CMIP6 scenarios,
91 and the state and evolution of the thermal imbalance of the permafrost (e.g.: Ji et al., 2022, Nitzbon
92 et al., 2023) in the considered region.

93 **2 Materials and methods**

94 *2.1 Study site: Kulingdakan, a forested catchment in continuous permafrost area*

95   The Kulingdakan catchment is located in the Krasnoïarsk Region (64.31°N, 100.28°E),
96 within a continuous permafrost zone, belonging to the boreal forest biome (Northern Taïga – see

4

97   Figure 1a). This pristine catchment is monitored for the study of boreal processes over past two
98   decades. The vegetation is dominated by larch (*Larix gmelinii*), dwarf shrubs, mosses and lichens.
99   The catchment covers an area of 41 km² and has an elevation ranging from 132 m to 630 m
100   (Prokushkin et al., 2004). The climate is cold and continental, with an average annual mean
101   temperature of -8°C and annual total precipitation of 400 mm (annual mean measured between
102   1999 and 2014 at the Tura meteorological station, 5 km south of the Kulingdakan catchment, 168 m
103   altitude). The stream, which flows from east to west, divides the 41 km^2 catchment area into two
104   approximately rectangular slopes of equal area, the North Aspect Slope (NAS) and the South
105   Aspect Slope (SAS). The hydrological budget in this watershed is largely dominated by
106   evapotranspiration fluxes (Orgogozo et al., 2019). Two horizons constitute the soil in the first few
107   meters: an organic horizon (duff) and a mineral horizon (mainly rocky/gravely loam).

108   Due to the difference in solar radiation induced by their aspect, primary production and
109   evapotranspiration are more intensive in SAS than in NAS. Thus the two slopes show significant
110   differences, in larch trees size and larch stands density, as well as in rooting depth, organic horizon
111   thickness and moss layer thickness. The thickness of the organic horizon is of 11.6 cm on the NAS
112   and 7.7 cm on the SAS (Gentsch, 2011), while the moss layer thickness is of 13 cm on the NAS and
113   6.4 cm on the SAS (Prokushkin et al., 2007). The rooting depth is of 10 cm into the mineral horizon
114   for NAS, and 60 cm for SAS (Viers et al., 2013), and this difference has been shown to be of great
115   importance for the dynamics of the active layer (Orgogozo et al., 2019). These pedological and
116   physiological contrasts between the two aspects of the watershed slope, summarized in Figure 1b,
117   must be considered when performing permafrost simulations (Supplementary material B).

5

118

119
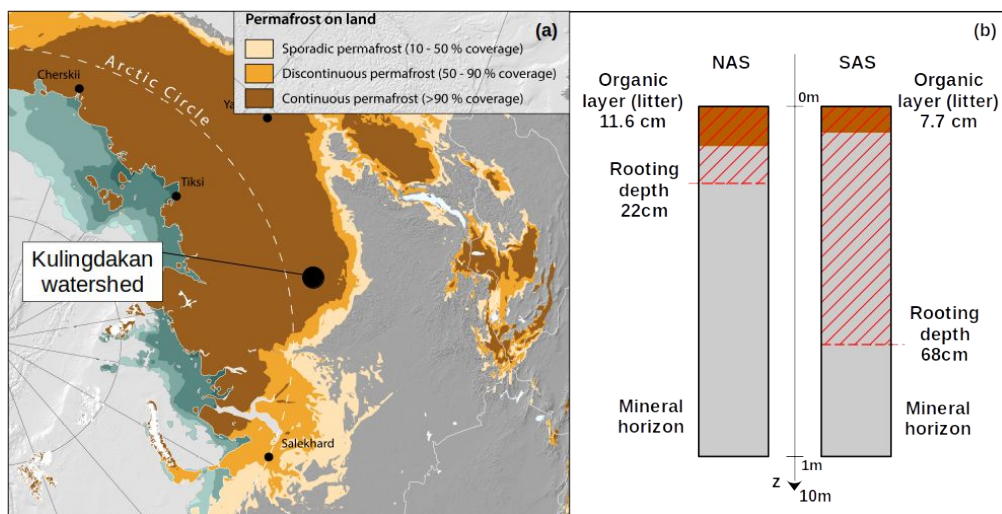
Figure 1: (a) Location of Kulingdakan watershed (map from GRID-Arendal/Nunataryuk). (b) Representation of soil column structure for North aspected slope (NAS) and South aspected slope (SAS) of the Kulingdakan watershed.

Previous modelling studies in the Kulingdakan catchment on water fluxes repartition, soil temperature at different depths and active layer thickness (Orgogozo et al., 2019, Orgogozo et al., 2023) demonstrated that the use of the permaFoam solver, together with boundary conditions (water fluxes and soil surface temperature) provided by field measurements, enabled to obtain numerical simulation results in agreement with in-situ observations under current climatic conditions .

2.2 The permaFoam cryohydrogeological simulator

The numerical tool used in this study is permaFoam (Orgogozo et al., 2019, 2023), the permafrost modelling solver developed in the framework of OpenFOAM, the open source, high performance computing tool box for computational fluid dynamics (Weller et al., 1998, openfoam.org, openfoam.com). This solver is designed to simulate 3D, transient coupled heat and water transfers in a variably saturated soil with evapotranspiration and freeze/thaw of the pore water. The two main equations solved by permaFoam are the Richards equation (1) that governs the flow of water and an energy balance equation (2) that governs the heat transfer, both defined at the Darcy scale of the considered porous medium (soil).

137

6

$$C_H(h)\frac{\partial h}{\partial t}=\nabla.\left(K_H(h,T).\nabla(h+z)\right)+Q_{AET}(h,t) \qquad (1)$$

$$\frac{\partial\left(\left(C_{T,eq}(h,T)+L\frac{\partial\theta_{ice}(h,T)}{\partial T}\right)T\right)}{\partial t}+\nabla.\left(V(h,T)C_{T,liquid}T\right)=\nabla.\left(K_{T,eq}(h,T)\nabla T\right) \qquad (2)$$

138

139 The two primary variables in equations (1) and (2) are the generalized water pressure head h [m]

140 and the soil temperature T [K], respectively. In Richards equation (1), z is the vertical coordinate

141 [m] (oriented upward), K_H is the hydraulic conductivity of the variably saturated, variably frozen

142 porous medium [m.s^{-1}], C_H is the capillary capacity (also called specific moisture capacity) of the

143 unsaturated porous medium [m^{-1}] and Q_{AET} [s^{-1}] is a source term representing the water uptake by

144 the vegetation through the evapotranspiration process (computed using Hamon formula, see Hamon

145 1963, Frolking, 1997). From the pressure head field h, the Darcy velocity V [m.s^{-1}] is derived

146 according to equation (3) :

$$V(h,T)=K_H(h,T).\nabla(h+z) \qquad (3)$$

147

148 In the energy balance equation (2), the considered transfer processes are conduction through the

149 entire porous medium, convection by pore water flow, and latent heat exchanges when phase

150 changes occurs. In this heat transfer equation, $K_{T,eq}$ [J.m^{-1}.s^{-1}.K^{-1}] is the apparent thermal

151 conductivity of the porous medium, θ_{ice} [-] is the volumetric ice content, L [J.m^{-3}] is the latent heat

152 of fusion of ice, $C_{T,eq}$ [J.m^{-3}K^{-1}] is the equivalent heat capacity of the porous medium, and $C_{T,liquid}$

153 [J.m^{-3}K^{-1}] is the equivalent heat capacity of liquid water. In permaFoam these two coupled equations

154 are solved in 3D using the finite volumes method, with sequential operator splitting for handling the

155 couplings, Picard loops for dealing with the non-linearities, and a backward time scheme for

156 temporal discretization. A detailed description of the solver and can be found in Orgogozo et al.

157 (2023).

158 The numerical resolution of these coupled and highly non-linear equations, including stiff

159 fronts generated by freeze/thaw processes, at the space and time scales required for studying climate

160 change impacts on boreal watersheds, requires both robust algorithm and efficient use of high

161 performance computing means. This is the reason why permaFoam is developed within the

162 OpenFOAM framework, which allows benefiting from up-to-date and efficient numerical methods

163 for solving partial differential equations on last generation supercomputing facilities. Thanks to its

7

164 implementation in OpenFOAM, the permaFoam solver has demonstrated excellent parallel
165 performances on various supercomputer architectures, both in terms of large numerical domains (up
166 to 1 billion mesh points on the CALMIP Olympe supercomputer) and number of cores (16,000 on
167 the GENCI IRENE-ROME supercomputer) (Orgogozo et al., 2023).

168 According to preliminary numerical experiments (data not shown), for modelling Kulingdakan
169 watershed permafrost the use of a dual 2D simplified representation, with a 2D transect for
170 representing each slope of the watershed (like in Orgogozo et al., 2019), does not induced
171 significant loss of information compared to full 3D modelling. Meanwhile, 3D simulations are far
172 more costly from a computational prospect than 2D simulation (Orgogozo et al., 2023). Besides, the
173 use of 2D simulations allows considering lateral transfers (Sjöberg et al., 2016, Lamontagne-Hallé
174 et al., 2018, Hamm and Frampton, 2021, Jan 2022). Thus in this paper we use 2D numerical
175 domains, with climatic forcing as top boundary conditions (see section 2.3) and geothermal heat
176 flux and nil water flux as bottom boundary conditions. The initial conditions were obtained by 10
177 years of spin-up under current climatic conditions. These current climatic conditions were
178 represented by a synthetic year of climate forcing corresponding to the multi-annual means of the
179 1999-2014 observations. The starting conditions of this spin-up were the extracted from results of
180 the previous calculations (Orgogozo et al., 2019). The convergence criterion for the spin-up was the
181 active layer thickness inter-annual difference (annual variability less than 0.2%).

182 The numerical simulations provide the full 2D fields of physical quantities describing the
183 heat and water flow within the both SAS and NAS (two 2.5 km wide, 10 m thick slopes), including
184 both frozen and active layer in each slope. These included soil temperature, pressure head, liquid
185 water content and ice content for each time step of saving (user defined, here each 6 months). In
186 addition, temperature, water content, ice content and evapotranspiration sink term are monitored at
187 hourly frequency throughout two vertical profiles located at mid-slope of SAS and NAS numerical
188 domains, using 61 virtual point probes distributed over the ten metres of the numerical domain
189 thickness. Finally, the infiltration and exfiltration water fluxes through the total soil surface are also
190 saved from the standard output at every time step.

191 This modelling set up is described in more details in Supplementary material B.

2.3 Soil surface conditions under climate change derived from CMIP6 scenarios

193 In order to apply climate forcing that are representative of possible future trajectories, we
194 consider climate scenarios produced as a part of the Coupled Model Intercomparison Project Phase

195 6 (CMIP6) organized by the Intergovernmental Panel on Climate Change (IPCC) (Eyring et al.,

196 2016), and in particular the so-called tier-1, key scenarios (O'Neill et al.,2016). These scenarios

197 have been highlighted because of their relevance to scientific questions, the range of possible

198 futures they cover, and their continuity with previous RCP scenarios (Representative Concentration

199 Pathways, van Vuuren et al., 2011) published during CMIP5. We considered four CMIP6 scenarios,

200 from the coldest to the hottest: SSP1-2.6, SSP2-4.5, SSP3-7.0 and SSP5-8.5. Among these scenario,

201 the SSP2-4.5 is most often used in permafrost studies (e.g.: Karjalainen et al., 2019, Ramage et al.,

202 2021, Hjort et al., 2022). For each of these scenarios, an ensemble of models has been run on

203 different regions of the globe. The climate model output data were accessed via the IPCC Working

204 Group I (IPCC-WGI) Interactive Atlas (Iturbide et al., 2021), February 2023 version, which

205 provides the median (P50) of the ensemble of models for a selected output variable, region and

206 scenarios. We used the air temperature and precipitation projections for the East Siberian region.

207 The temporal evolution of their annual means between 2015 and 2100 have been summed to the

208 multi-annual (1999-2014) yearly averages measured in Tura, for obtaining the local scenarios of

209 climate change to be considered in this work (Fig. 2).

210

211
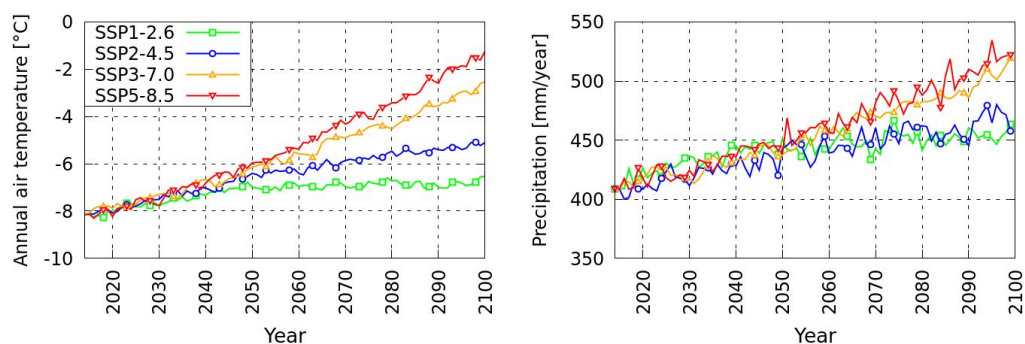
Figure 2: Projections of air temperature and precipitation in Kulingdakan based on CMIP6 projections on the Eastern Siberia area.

214 The projections show an increase in air temperature over the century, with a rate between

215 +1.9 °C/100 yr (SSP1-2.6) and +7.8 °C/100 yr (SSP5-8.5), which is for every scenario higher than

216 the global rate of increase (Fan et al., 2020). Annual precipitation could also change significantly,

217 with a relative increase in 2100 of +12% (SSP1-2.6) to +29% (SSP5-8.5) compared to current

218 value.

9

219   In order to translate these climate projections, that describe atmospheric conditions, into
220 suitable soil surface boundary conditions for cryohydrogeological simulations (water fluxes and
221 temperature at the soil surface, beneath snow and moss layer), a dedicated empirical procedure has
222 been developed. The goal is to set up a methodology for deriving soil surface temperature from air
223 temperature in the slopes of Kulingdakan watershed, based on the available observation data.
224 Indeed, soil temperature and air temperature may be significantly different in such a boreal forest
225 environment, due to the effects of understory (Zellweger et al., 2019, Haesen et al., 2021), moss
226 cover insulation (Blok et al., 2011, Cazaurang et al., 2023), the winter snowpack (Jan and Painter,
227 2020, Khani et al., 2023) and its interactions with vegetation (Dominé et al., 2022). This empirical,
228 site-specific procedure is detailed in Supplementary material A, and it allows to build up a slope-
229 wise soil temperature estimates on the basis of air temperature and snow conditions. For water
230 fluxes, the simplest approximation has been adopted, assuming that the water flux at the top of the
231 soil is equal to the rain flux. For soil surface temperature estimate, we first used a modified
232 temperature index approach (Braithwaite and Olesen, 1989, Hock 2003) for estimating snow water
233 equivalent, and then a multiple regression for deriving below moss, soil surface temperature from
234 air temperature, precipitation and snow water equivalent.

235   We chose a temperature index approach to simulate the snow water equivalent on the soil
236 surface because climate projections only provide air temperature and precipitation, whereas a more
237 advanced energy balance snowpack model requires additional information on wind, radiation, and
238 air humidity. To calibrate this temperature index model we first reconstructed the snow water
239 equivalent for the period 1999-2014 from the observed snow depth with the Multiple Snow Data
240 Assimilation System (MuSA) toolbox (Alonso-González et al., 2022) forced with ERA5 data
241 (Hersbach et al., 2020), fusing available snow depth observations with an ensemble of simulations
242 generated by the energy and mass balance model the Flexible Snow Model (Essery, 2015)). The
243 SWE model shows a good agreement with the MuSA reconstructions (Figure 3a), hence this model
244 was used to estimate SWE under future climate projections (Figure 3b).

245
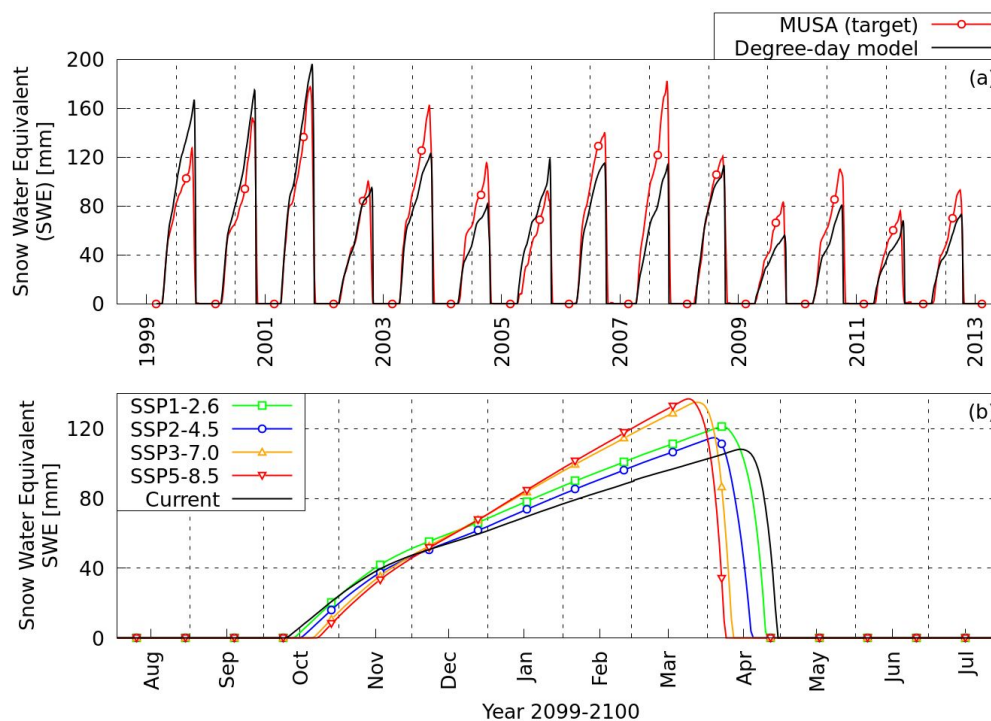
Figure 3: Present snow model comparison with MuSA output (a) and projection at the end of the century (b)

Then, we calibrate a multiple regression to derive soil surface temperature as a function of air temperature, while taking into account moss and snow layers insulating effect. Calibrations are performed with air temperature and precipitation data measurements and MuSA derived snow water equivalent between 1999 and 2014, and top soil (i.e., below moss) temperature measured in situ between 2003 and 2005. With this procedure, for each slope, an empirical transfer function that provides soil temperature estimates derived from air temperature and precipitation is obtained. These empirical transfer functions are in good agreement with the observation, as shown on Figure 4.
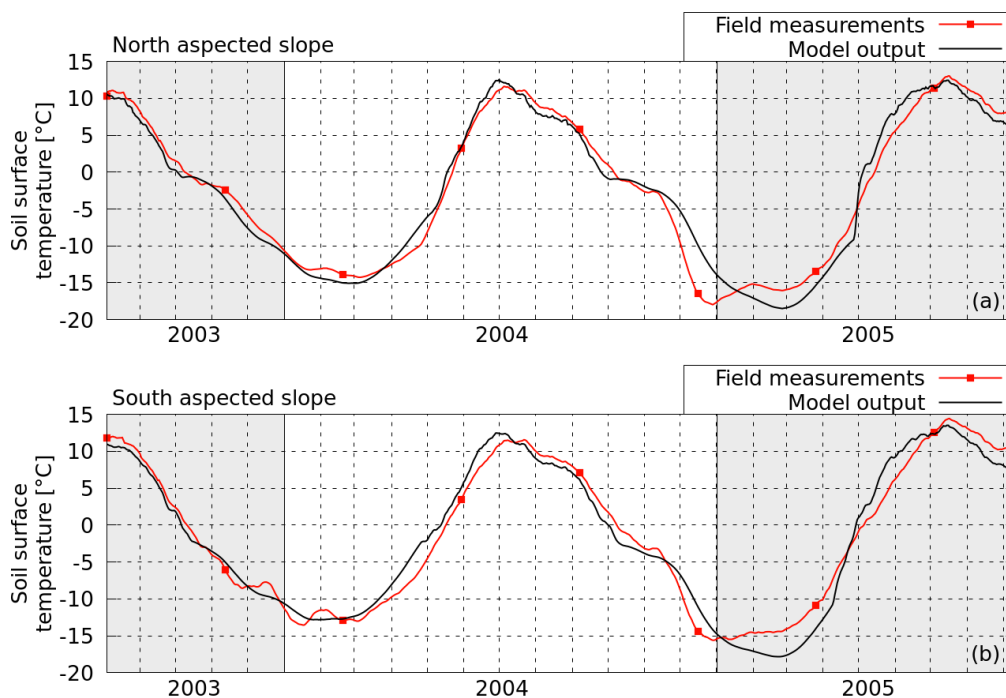
**Figure 4: Measurements and empirical transfer function estimates for soil surface temperature in present climatic conditions in NAS (a) and in SAS (b).**

Finally, these transfer functions are used to produce scenarios of soil surface temperature under climate change for the two slopes of the catchment (Fig. 5). This information is needed for building the soil surface boundary conditions of the hydrogeological simulations.

12
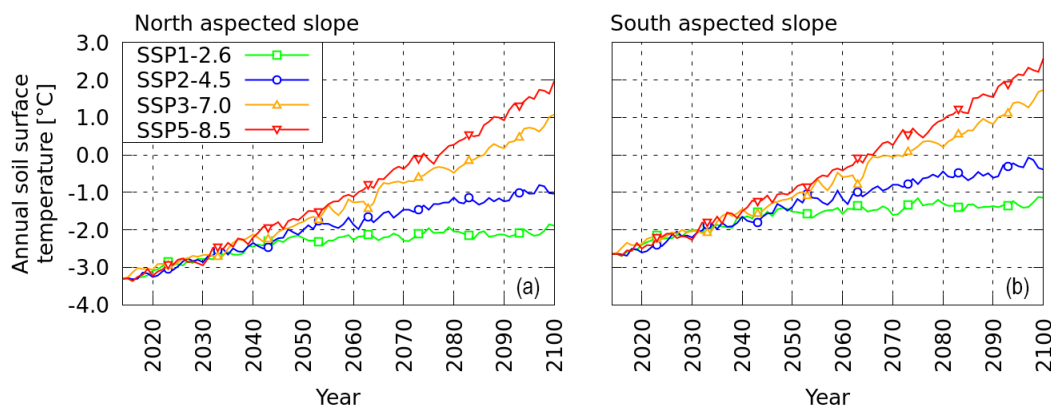
Figure 5: Soil surface temperature projections over the century based on SSP scenarios obtained using transfer function described in Supplementary material A. Transfer function model estimation for soil surface temperature at present conditions for north aspected slope (a) and south aspected slope of the Kulingdakan watershed(b).

The four projections based on the different SSP scenarios lead to an increase of the ground surface temperature from +1.4°C (SSP1-2.6) to +5.2°C (SSP5-8.5) between 2014 and 2100 (Fig. 5a and 5b). These rates of increase, roughly equivalent by extrapolation to +1.7°C/100 yrs (SSP1-2.6) and +5.9°C/100yrs (SSP-8.5), are lower than the observed increases in air temperature (+1.9°C/100yr for SSP1-2.6 and +7.8°C/100 yr for SSP5-8.5) due to the insulating effect of the snow cover and the vegetation layer, and also due to the thermal inertia of the soil column below the surface. One can note that for SSP3-7.0 and SSP5-8.5 scenarios, the mean annual soil surface temperature becomes positive around 2080. It must be emphasized that our empirical approach was based on parametrical fitting on observation data for estimating the transfer function between atmospheric forcing and soil surface temperature. As a result, no vegetation changes along climate change could be considered in this transfer function. Therefore, we focus on purely physical response of the catchment permafrost to climate change, taking into account vegetation impacts on permafrost dynamics at constant vegetation cover. Using an empirical transfer function for getting soil surface temperature signal from atmospheric conditions under climate change poses the problem of extrapolation, for instance in extreme hot weather conditions that may occur in the future, being unprecedented in the training period 1999-2014. However, performing mechanistic modelling of surface energy balance in extreme weather conditions under permafrost contexts was beyond the scope of this work.

13

290 *2.4 High Performance Computing methodology*

291   Despite the use of the 2D assumption and the excellent parallel performance of the

292 permaFoam solver, carrying out a mechanistic permafrost dynamics simulation at the scale of the

293 catchment over almost a century remains a particular computational challenge. This section outlines

294 some elements of the methodology and computing means used to meet this challenge.

295   The calculations are carried out on the IRENE JOLIOT-CURIE supercomputer operated by

296 the French Alternative Energies and Atomic Energy Commission (CEA). This supercomputer

297 offers, among other partitions, an AMD partition equipped with AMD Rome (Epyc) processors,

298 with 64 computational cores each. OpenFOAM is used in this work only on CPUs with the MPI

299 communication protocol. Since the mesh domain is composed by 525k cells for each slope

300 (sufficient for convergence, see Supplementary material B), the number of MPI processes can be

301 kept relatively low, with the use of 256 MPI-processes for each case treated here. Like most of fluid

302 mechanics solvers based on finite volumes discretization, permaFoam exhibits a memory-bound

303 nature in most of its operations, with low arithmetic intensity. Therefore, we adapted the use of the

304 supercomputing infrastructure by depopulating the compute nodes by a factor of two (using only 32

305 computational cores out of the 64 cores available on each processor), thus largely broadening the

306 bandwidth available for each MPI process. This operation reduced the computation time by almost

307 a factor of two without requiring significantly higher CPU hour costs.

308

309   As a whole, the computational campaign required the use of 1.8 million CPU hours,

310 generated almost 2TB of raw data and produced ~80k inodes, with a restitution time of

311 approximately one month for each simulation (i.e.: for one scenario and for one slope).

312 **3 Results**

313

314 Post-processing the computed 2D fields of physical quantities describing the heat and water flow

315 within the both SAS and NAS (two 2.5 km wide, 10 m thick slopes), including both frozen and

316 active layer in each slope, a large wealth of data characterizing the considered virtual permafrost

317 dynamics is obtained (Supplementary material C), and below, only key features of the centennial

318 evolution under climate change are presented.

14

3.1 Trends in soil temperatures

319

320   Soil temperature at different depth is one of the key variable for characterizing permafrost

321 dynamics. The multi-annual trends induced by climate warming of the mean annual soil

322 temperature between 2014 and 2100 at 3 depths (10 cm, 1 m and 5 m below the surface) are

323 illustrated in Figure 6.

324
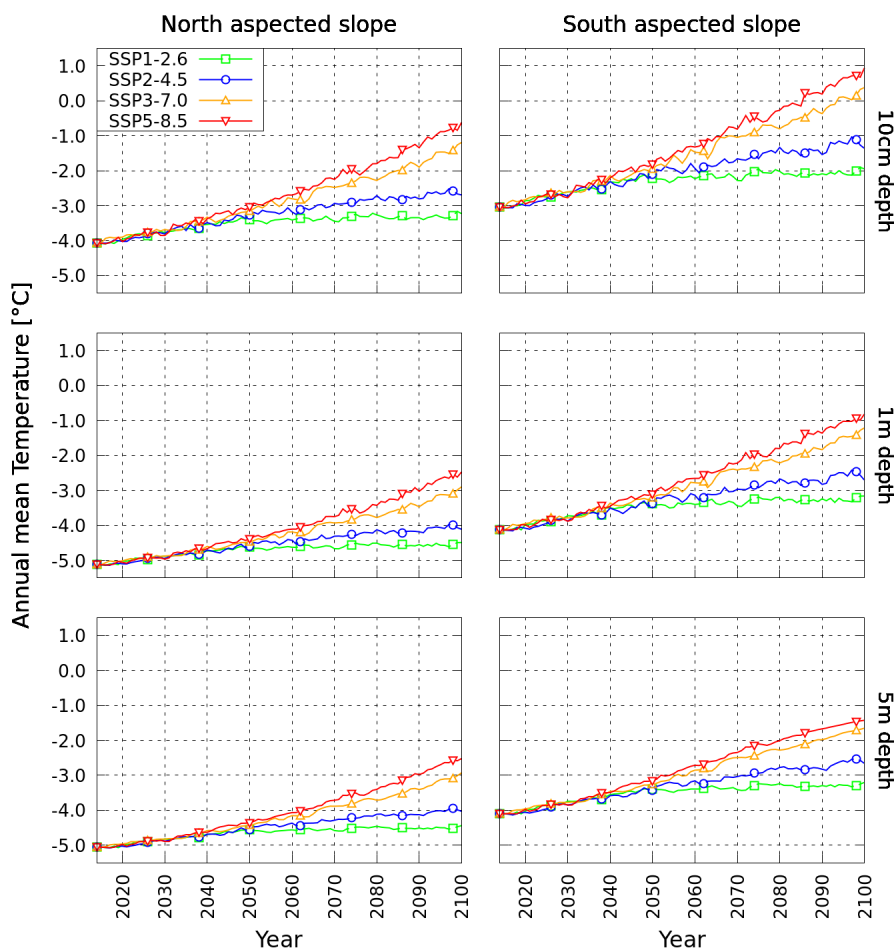
Figure 6: Mean annual temperature evolution at 10cm,1m and 5m under the surface for each scenario and slope considered.

328   In both slopes, the soil temperature experiences significant increase down to 5 m depth, for

329   all climate warming scenario considered. The annual mean soil temperature becomes even positive

330   close to the surface in the SAS for the two hottest scenarios, by 2085 with SSP5-8.5 and by 2095

331   with SSP3-7.0. Meanwhile, for the medium scenario SSP2-4.5 and for the coldest scenario SSP1-

332   2.6, the mean annual soil temperature stay everywhere negative until 2100. The warming is more

333   intensive in the SAS than in the NAS, and, as expected, the amplitude of soil warming decreases

334   with depth. In SAS, at 10 cm depth the temperature rise between current conditions and the year

335   2100 is 1 °C for the SSP1-2.6 scenario and 4 °C for the SSP5-8.5 scenario, while at 5 m depth, the

336   temperature rises are 0.9 and 2.7 °C, respectively. In NAS, at 10 cm depth the temperature rise

337   between current conditions and the year 2100 is of 0.8 °C for the SSP1-2.6 scenario and of 3.4 °C

338   for the SSP5-8.5 scenario, while at 5 m depth, the temperature rises are 0.6 and 2.5°C respectively.

339   It should be noted that, for both slopes, the vertical gradient of temperature in 2100 is higher in

340   scenario SSP5-8.5 than in scenario SSP1-2.6. This indicates a stronger thermal non-equilibrium

341   under more intense warming. For instance, the difference of temperature between 10 cm and 5 m

342   depth is 2.3 °C in SAS and of 1.9 °C in NAS for scenario SSP5-8.5, while it is 1.2 °C in both SAS

343   and NAS for the SSP1-2.6 scenario. In order to provide insight into the thermal equilibrium state of

344   the soil columns in each slope in 2100, the vertical temperature profiles for this year are plotted for

345   each scenario in Figure 7. For further investigating the distance from equilibrium state in each

346   slope, an additional numerical experiment has been performed by simulating 30 years more at the

347   2100 climatic conditions, and the obtained vertical temperature profiles are shown in Figure 7.

348
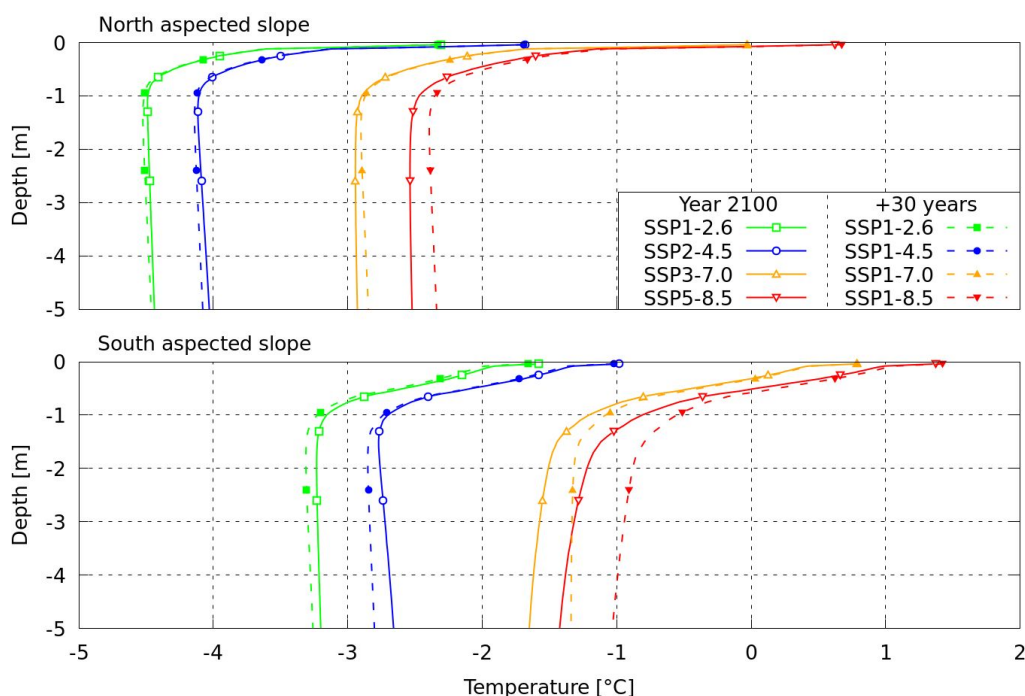
Figure 7: Annual mean temperature profiles in 2100 and after 30 years of additional cycling of the climatic forcing of this last year.

Considering the soil temperature profiles in 2100, two regions may be distinguished: the first meter with steep positive vertical gradients (the soil surface is warmer than the bottom of the active layer), and a deeper region, with smoother vertical thermal gradients, either slightly negative (SSP1-2.6 and SSP2-4.5 in NAS and SAS), almost nil (SSP3-7.0 and SSP5-8.5 in NAS) or positive (SSP3-7.0 and SSP5-8.5 in SAS). When comparing these profiles with those obtained with 30 additional years of modelling in constant '2100' climatic conditions, we observe important differences in both slopes for scenario SSP5-8.5, and also for scenario SSP3-7.0 and scenario SSP2-4.5 in SAS.

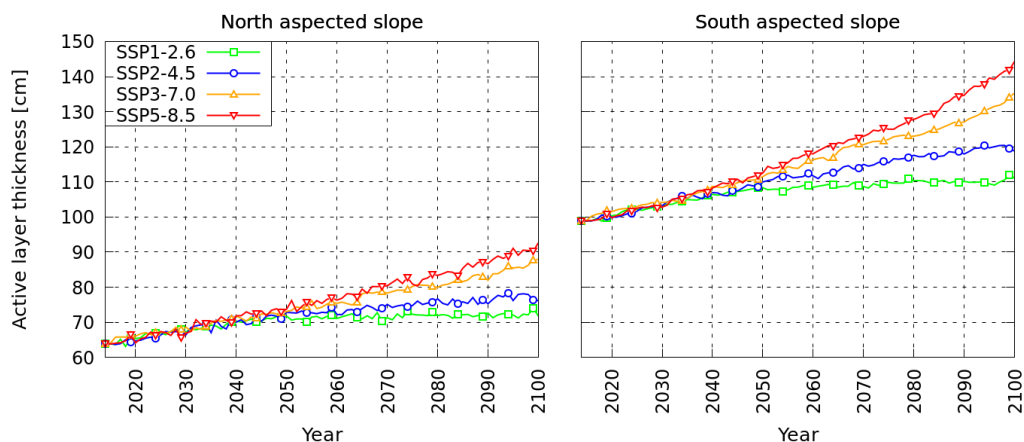### 3.2 Active layer thickness evolution

Numerical simulations give access to soil temperature at various depth. From soil temperature profile, the maximum depth with a positive temperature may be computed at each time

17

365   step. The maximum thawed depth obtained over a year defines the active layer thickness (ALT) of

366   this year. Active layer thickness has been computed for each scenario and each year and is plotted

367   for both NAS and SAS in Figure 8.

368

369

370   **Figure 8: Active layer thickness temporal evolution on North (left) and South (right) aspect**
371   **Slope of the Kulingdakan watershed obtained from permaFoam simulations under different**
372   **SSP scenarios.**

373

374   For both slopes, an increase in active layer thickness is observed between 2014 and 2100 in every

375   scenario, with a more important thickening in SAS than in NAS. SSP1-2.6 leads to an increase of

376   +12.3 cm/+12% for SAS and of +7.9 cm / +12% for NAS, while SSP5-8.5 leads to a more dramatic

377   increase of +45 cm / +46% for SAS and of +29 cm / +45% for NAS. In the first half of the century,

378   the behavior of active layer thickness does not differ significantly between scenarios, with a

379   thickening rate in ALT of about +3.3 mm/year (±21%) in SAS and of +2.5 mm/year (±19%) in

380   NAS. However, in the second half of the century (2050-2100), different scenarios lead to very

381   different active layer thickness evolution dynamics. For SSP1-2.6, the thickening rate is rather

382   small, with a rate of +0.52 mm/year for SAS and +0.25 mm/year for NAS, while for SSP5-8.5

383   scenario, the thickening rate rises to +5.8 mm/year for SAS and +3.5 mm/year for NAS. By the end

384   of the simulated period, these thickening rates show no diminishing trend in SAS, suggesting that

385   the dynamic thermal equilibrium is not reached in the active layer. For illustrating this, Figure 9

386   shows the active layer thickness evolution for 30 years of additional simulations while keeping the

387   climatic conditions of 2100 for each scenario.

18

388
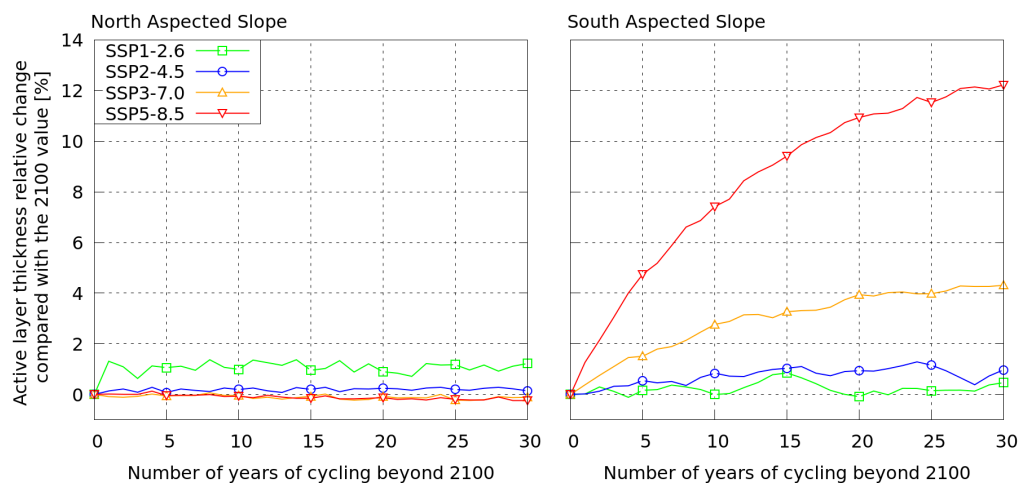
389
390 **Figure 9: Relative change in active layer thickness compared with the year 2100 over 30 years**
391 **of spin-up of the 2100 climatic conditions.**

392

393 Overall, the active layer is not far from thermal equilibrium in both slope for the coldest (SSP1-2.6)
394 and medium (SSP2-4.5) climatic scenarios. However, when considering the hottest SSP5-8.5
395 scenario, an important thermal inertia effect appears in SAS, with an additional active layer
396 thickness increase over these 30 years of +12.6 % compared to the 2100 value, i.e. an increase of
397 +18 cm. This additional change in active layer thickness brings the resulting change compared to
398 2014 value to +63 cm (+64%) for the hottest scenario.

399

400

19

3.3 Trends in soil moisture

401

402   Soil moisture content experienced less important changes than thermal regime under the

403   considered climate change scenario. For illustrating the soil moisture evolution near the surface, the

404   total water, liquid water and ice volumetric contents have been averaged over the first 2 m of the

405   soil for each slopes, and their 2014-2100 evolution have been plotted on Figure 10 for the four

406   climatic scenarios. Regardless of the scenario, there is no significant evolution of total water content

407   in the first two meters of soil in NAS, and the only noticeable change is the increase in proportion

408   of liquid water (+15 % in SSP1-2.6, +24 % in SSP2-4.5, +49% in SSP3-7.0, +60 % in SSP5-8.5),

409   suggesting an increase in the amount of liquid water available for vegetation. In SAS however, the

410   first two meters of the soil exhibited a slight but detectable diminishing of total water content by

411   2100 (-5 % in SSP1-2.6 and SSP2-4.5, -10% in SSP3-7.0, -11 % in SSP5-8.5). On the other hand

412   the proportion of liquid water over ice increases (+7 % in SSP1-2.6, +16 % in SSP2-4.5, +38% in

413   SSP3-7.0, +51 % in SSP5-8.5). Therefore, in SAS slope, climate warming may result in no

414   significant changes in the amount of liquid water available for vegetation. It should be emphasized

415   that the presented partitioning between liquid water and ice is based on the mean annual quantities.

416   This provides considerably smaller proportion of liquid water compared to that in the end of the

417   active season (second half of September), when active layer is at its maximum thickness.

20

418
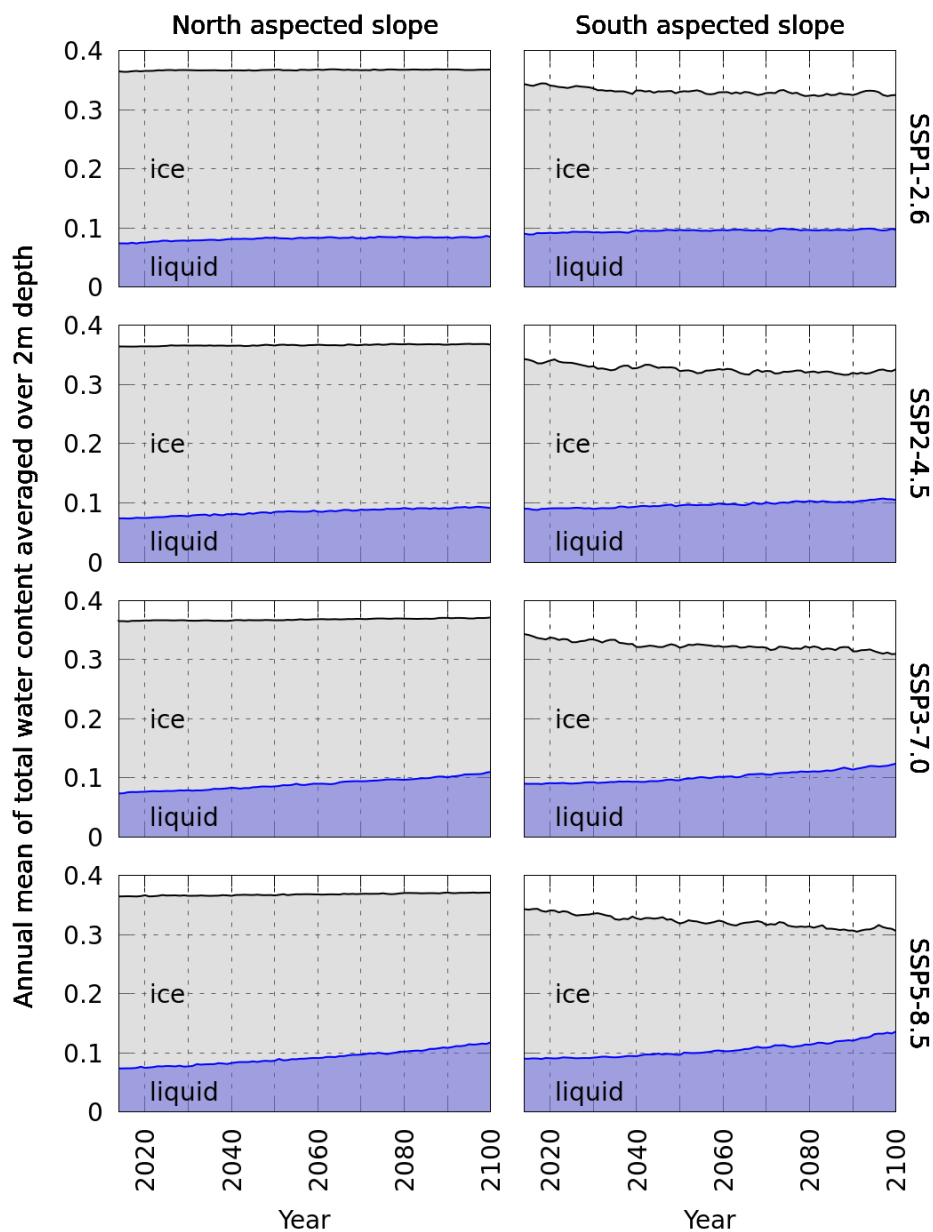
Figure 10: Annual mean of total water content [m^3 of water / m^3 of soil], liquid water content and ice content averaged over 2m depth in different climate projections.

421

422

In order to investigate the local variation of moisture content in the rooting zone and in the active layers of each slopes, the vertical profiles of mean annual total water content have been plotted on Figure 11 for current climatic conditions and for year 2100 under SSP1-2.6, SSP2-4.5, SSP3-7.0 and SSP5-8.5 scenarios. The water profiles do not change significantly in the highly porous organic horizon in both slopes. In the mineral horizon, the behavior of SAS and NAS get more contrasted, due to downward vertical moisture gradients (and thus upward water movements) in NAS and upward vertical moisture gradients (and thus downward water movements) in SAS. In NAS, the only evolution with climate change is a thickening of the zone with a downward vertical moisture gradient (i.e., an upward water flux) alongside the thickening of the active layer, with no significant changes of the gradient itself. Meanwhile, in SAS, alongside with the thickening of the zone with water movements (i.e. moisture gradients) that comes with active layer thickening, significant changes of the upward moisture gradients are expected to occur: the hotter the scenario, the steeper the gradients, and thus the stronger the downward water fluxes.

436
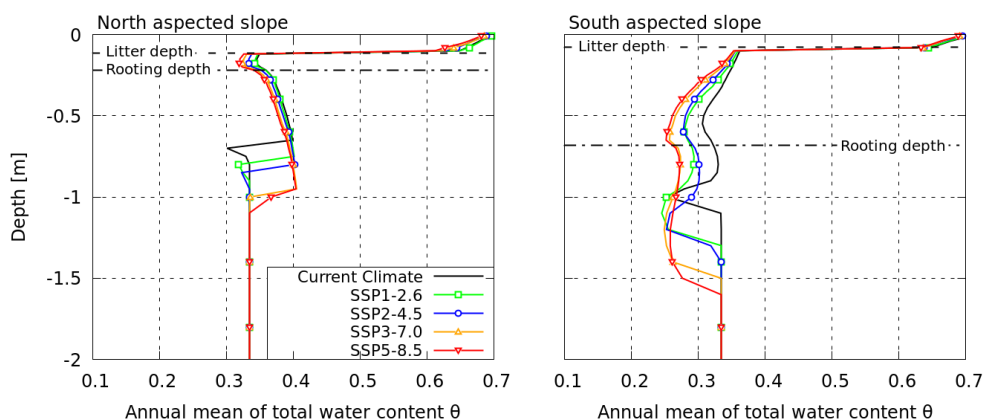
Figure 11: 2m-depth profiles of annual mean of total water content [m^3 of water / m^3 of soil] in 2100: projections compared to current state.

439

3.4 Water fluxes

The water fluxes also significantly change along with climate change in both slopes for every scenario. Evapotranspiration is the most important component of the hydrological budget in Kulingdakan. Focusing on this dominant component, Figure 12 presents the centennial evolution of evapotranspiration in both slopes and of precipitation for the fourth considered climate change scenarios. A significant increase of evapotranspiration is simulated in all cases, with an increase between +18 mm/+5% (SSP1-2.6) and +94 mm/+26% (SSP5-8.5) in SAS, and between +40mm/+11% and +100 mm/+29% in NAS. The increase of the evapotranspiration fluxes in Kulingdakan are closely correlated to the increase of precipitation, with similar increase rates for both slopes.

450

451
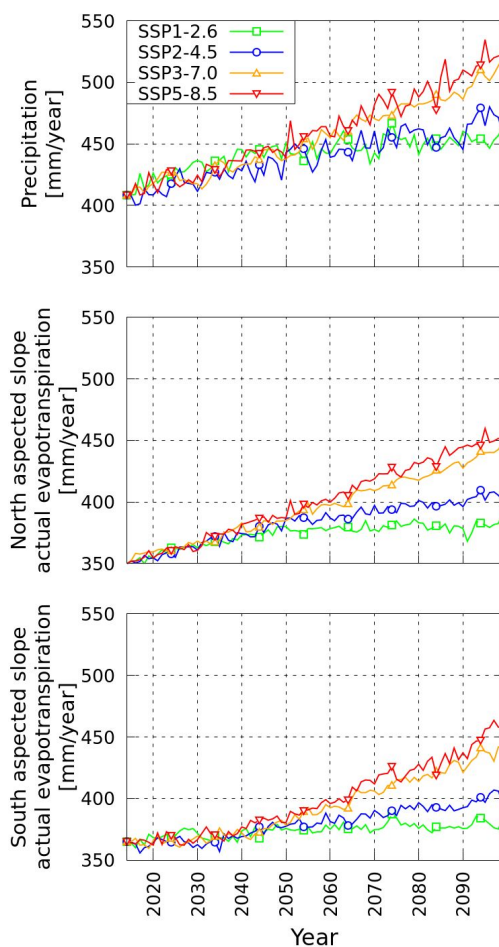
Figure 12: Precipitation and actual evapotranspiration evolution over the century

Once again, the evolution is globally similar among scenarios until 2050, with significant divergences appearing only between 2050 and 2100.

455

4 Discussion

The numerical results obtained by mechanistical modelling of heat and water transfer within the permafrost and active layer of Kulingdakan document the physical response to be expected by this catchment under climate change, with soil warming (Figure 6) and active layer thickening (Figure 8) in all climate scenarios. An important spatial variability of this thermal response is identified, in relation with the aspect of the slopes, which stems from sizable contrast in vegetation cover, hydrologic and thermal state and active layer dynamics as currently observed between the two slopes (Prokushkin et al. 2007). Indeed, since the NAS is wetter, its thermal inertia is more important due to the largest amount of latent heat that must be provided to thaw and warm its soils, compared to the drier soils of the SAS. This difference in moisture content is largely due to the difference in their tree cover biomass and physiology, i.e. the deeper root layer in SAS compared to NAS induces more intensive evapotranspiration in the former, both under current (Orgogozo et al., 2019) and future climate conditions. Note that this contrast tends to diminish with climate warming (Figure 12). Nonetheless, according to the performed simulations, the SAS will stay drier than NAS with climate warming (Figure 10). The structure of water fluxes within the active layer, with an upward flux to the thinner, close to the surface root layer in NAS and a downward flux toward the bottom of the thicker root layer in SAS is also preserved under climate change, with an intensification of the fluxes in SAS under the hottest scenarios (Figure 11). Further, the thicker moss layer in NAS is likely to dampen more efficiently the effect of changes in the climatic conditions on soil compared to the thinner one of the SAS. Because our modelling takes into account the root water uptake mechanistically (Orgogozo et al., 2023) and the low vegetation insulating effect empirically (Supplementary material A), the warming of the soil and the thickening of the active layer under climate change is significantly more pronounced in SAS than in NAS. This persistent local spatial variability in permafrost dynamics reflects the prominent role of micro-climatic condition in responses of forest environments to climate change that has been demonstrated recently in the literature (Zellweger et al., 2020). It must be emphasized that all these numerical results have been obtained considering the vegetation in its present state. Strong local variability of the vegetation cover depending on the permafrost conditions in Kulingdakan catchment (Orgogozo et al., 2019) and in a broader perspective in the entire Arctic (Oehri et al., 2022) is consistent with important interplay between vegetation evolution under climate change (e.g. Vitasse et al. 2009, 2011, Rew et al., 2020) and permafrost pattern, which has not been explicitly considered in this

study. At the centennial time scale, changes in the tree growth rate, the forest fire frequency or the nature of the vegetation cover may exert important impacts on permafrost conditions (Cable et al., 2016; Fedorov et al., 2019; Rew et al., 2020; Li et al., 2021; Heijmans et al., 2022). Meanwhile, without belittling these probably important and complex interactions between vegetation dynamics and permafrost dynamics, this study shows that important impacts of climate change are to be expected on permafrost dynamics of the forested continuous permafrost area even at steady vegetation cover. We noted that the more intense the climate change, the more pronounced these thermal responses. For instance, under the hottest SSP5-8.5 scenario, a maximum evolution of the active layer thickness is +45 cm/+46% for SAS and +28 cm/+44% for NAS, while in the medium SSP2-4.5 scenario, an increase of +20 cm/+20% for SAS and of +12 cm/+19% for NAS is anticipated.

To produce a broader geographical context of the simulated active layer thickening at the scale of a small catchment, a comparison of these centennial evolutions under climate change with large geographical coverage is performed in Figure 13.
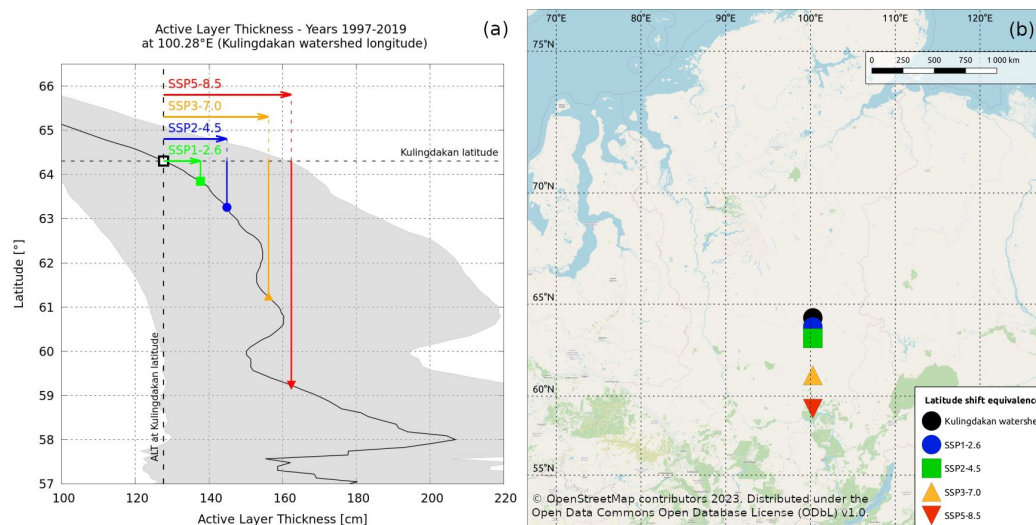
Figure 13: (a) Equivalence between simulated active layer thickening by 2100 under climate change (SAS and NAS average) and southward latitudinal shift in current climatic conditions (1997-2019). – latitudinal trend (black line - average over a 1°lat. × 1°long. polygon) and envelops (in grey - min/max over year within the same polygon) extracted from Permafrost_cci (Obu et al., 2021). (b) Representation of the latitudinal southward shift equivalent to each climate scenario's active layer thickening on the regional map.

The simulated thickening of the active layer, averaged over both slopes of Kulingdakan, are depicted as southward latitudinal shifts along the meridian passing by Kulingdakan, i.e. with a pure North-South translation along the 100.28 °E (Fig. 13). The latitudinal evolution of the active layer thickness along the current meridian is computed based on the permafrost_CCI dataset (Obu et al., 2021), by averaging the value of the multi-annual mean of active layer thickness for the 1997-2019 period over a polygon of 1° latitude by 1° of longitude centered on the considered meridian and browsing the latitudes 67°N and 57°N. It can be seen that, in the hottest scenario SSP5-8.5, the active layer thickening would correspond to a 560 km southward shift, while in the medium scenario SSP2-4.5, it would correspond to a 120 km southward shift.

Under a permanently changing climatic context, an important question is the state of thermal equilibrium versus non-equilibrium of the permafrost (Obu et al., 2019): is the climate change induced warming slow enough so that permafrost may be considered at every time close to the thermal equilibrium with climatic conditions, or on the contrary, the transient effects dominate the thermal dynamics of permafrost under climate change? The simulation results of this work provide information for characterizing the degree of thermal equilibrium of the continuous permafrost, in a forested study site under various scenarios of climate change. First of all, we emphasize that, since the bottom thermal boundary condition in our modelling is geothermal heat flux (Duchkov et al., 1997), the assumption of overall thermal equilibrium in depth (< 10 m) in the hundreds of meter of thick permafrost of the Putorana plateau (Pokrovsky et al., 2005) is implicitly made. Meanwhile, the temperature profiles shown in Figure 7 demonstrate that under this assumption the thermal equilibrium state of the first 10 m of soil in 2100 depends on both the climate change scenario and the slope aspect. In NAS, thermal equilibrium of the first 10m of soil is achieved by 2100 in every climate scenario, with only a slight shift between 2100 and (2100 +30) conditions in SSP5-8.5 scenario. Besides, with sub-zero vertical thermal gradients in each scenario, only small heat exchanges between surface and depth occur. On the contrary, by 2100 in SAS strong thermal non-equilibrium is encountered in the two hottest scenarios, SSP3-7.0 and SSP5-8.5 (Figures 7 and 8). Under these scenarios, sizable evolutions of temperature profiles are expected to occur between 2100 and 2100+30. Moreover, for these two hottest scenarios, the vertical thermal gradient between 1 and 10m depth are clearly positive (considering an upward vertical axis), which implies an ongoing heat flux from the surface to the depth. In this case, the permafrost is warming below 10m, at a rate that we implicitly assume to be small enough so that it does not modify the total amount of heat stored within this deep permafrost. As such, in scenarios SSP3-7.0 and SSP5-8.5, the climate

27

warming clearly induces transient warming of the permafrost in depth (below 10m) in the south aspect slopes of the Kulingdakan watershed. One could note a slightly decreasing trends in the soil temperature under scenarios SSP1-2.6 and SSP2-4.5. This is due to inter-annual variabilities in both precipitation and air temperature in CMIP6 projections (Figure 2). Therefore, the year 2100, which is repeated over 30 cycles to assess the equilibrium state of the permafrost, may offer different conditions from those observed in the previous decade 2090-2100. For example, in SSP2-4.5, the last decade experiences an important annual precipitation peak, up to 475mm/year, centered around 2095, before a decreasing trend on the second part of the decade ending up to a precipitation of 410mm/year projected in 2100. This results for the year 2100 in a decrease of the snow cover insulating effect in winter, and thus a cooling of soil surface temperature (Fig. 5), compared to the conditions encountered in the previous decade,

Overall, results of the present study may be used to improve our understanding of the climate warming-related changes in the wide areas of boreal forest on continuous permafrost, with strong implications for continental surfaces (Revich et al., 2022), ecosystems (Wang and Liu 2022) and element cycles (Schuur et al., 2022) there, and related global consequences and feedbacks. The use of mechanistic modelling, although computationally costly, is capable of providing quantitative information for feeding these research fields. This approach will be applied in other environmentally monitored boreal watershed in the near future, in order to numerically characterize the physical response of permafrost to climate change in various representative permafrost context, for instance in Northern Sweden (Auda et al., 2023) and Western Siberia (Cazaurang et al., 2023).

5 Conclusion

Four main conclusions that could be drawn from this numerical study are the following:

- All climate change scenarios trigger significant soil warming (+1.5°C in SAS and +1°C in NAS under SSP2-4.5 scenario at 1 meter depth according to the presented simulations) and an increase in the active layers thickness (+20 cm/+20% in SAS and +12 cm/+19% in NAS under SSP2-4.5 scenario) in both slopes of the Kulingdakan watershed.

- For all climate change scenarios, the combination of soil warming and precipitation increase leads to an important increase in evapotranspiration in both slopes (+34 mm/+9% in SAS and +52 mm/+15% in NAS under SSP2-4.5 scenario). Meanwhile, the mean annual soil moisture decreases only slightly in NAS (-2.3% under SSP2-4.5 scenario, averaged over the 22 cm of rooting depth),

28

but it is more pronounced in SAS (-5,6% in NAS under SSP2-4.5 scenario, averaged over the 68 cm of rooting depth).

- Important spatial variability observed in the Kulingdakan watershed illustrate the key role of meso-climatic conditions and small-scale geomorphological contrasts in permafrost response to climate warming

- Under the two hottest scenarios of climate change SSP3-7.0 and SSP5-8.5, the near-surface permafrost of the SAS of the Kulingdakan watershed are in non-equilibrium thermal state in 2100, and further investigation is needed to assess whether or not the permafrost underneath 10m depth will be close to thermal equilibrium in this region. This advocates the need of developing non-equilibrium modelling approaches for regional and global permafrost modelling under climate change.

The approach developed in this study can be applied to other high-latitude permafrost-affected catchments, provided that necessary information on current thermal and hydrological parameters of soil as well as vegetation coverage are available.

Competing interests

The contact author has declared that none of the authors has any competing interests.

Acknowledgments

References

594 Alonso-González E., Aalstad K., Baba M. W., Revuelto J., López-Moreno J. I., Fiddes J., Essery R.,

595 Gascoin, S.: The Multiple Snow Data Assimilation System (MuSA v1.0), Geosci. Model Dev., 15,

596 9127–9155, doi:10.5194/gmd-15-9127-2022, 2022.

597

598 Arndal M.F. and Topp-Jørgensen E. (Eds.), INTERACT Station Catalogue – 2020. DCE – Danish

599 Centre for Environment and Energy, Aarhus University, Denmark. 190 p, ISBN: 978-87-93129-15-

600 3, www.eu-interact.org, 2020.

601

602 Auda Y., Lundin E.J., Gustafsson J., Pokrovsky O.S., Cazaurang S., Orgogozo L.: A New Land

603 Cover Map of Two Watersheds under Long-Term Environmental Monitoring in the Swedish Arctic

604 Using Sentinel-2 Data. *Water, 15*, 3311. doi:10.3390/w15183311, 2023.

605

606 Bartsch A. Pointner G., Nitze I., Efimova A., Jakober D., Ley S., Högström E., Grosse G.,

607 Schweitzer P., Expanding infrastructure and growing anthropogenic impacts along Arctic coasts,

608 *Environ. Res. Lett.* **16** 115013, doi:10.1088/1748-9326/ac3176, 2021.

609

610 Blok D., Heijmans M.M.P.D., Schaepman-Strub G., Van Ruijven F., Parmentier F.J.W and

611 Maximov T.C: The Cooling Capacity of Mosses: Controls on Water and Energy Fluxes in a

612 Siberian Tundra Site, *Ecosystems* **14**, 1055–1065, doi:10.1007/s10021-011-9463-5, 2011.

613

614 Braithwaite R. J., Olesen O. B.: Calculation of glacier ablation from air temperature, West

615 Greenland. In Glacier fluctuations and climatic change, J. Oerlemans ed., pp. 219-233, Kluwer

616 Academic Publishers, 1989.

617

618 Biskaborn B.K., Smith S.L., Noetzli J. *et al.* Permafrost is warming at a global scale. *Nat Commun*

619 **10**, 264, doi:10.1038/s41467-018-08240-4, 2019.

620

621 Cable W. L., Romanovsky V. E. and Jorgenson, M. T.: Scaling-up permafrost thermal

622 measurements in western Alaska using an ecotype approach, The Cryosphere, 10, 2517–2532,

623 doi:10.5194/tc-10-2517-2016, 2016.

624

626   Cazaurang, S., Marcoux M., Pokrovsky O. S., Loiko S. V., Lim A. G., Audry, S., Shirokova, L. S.,

627   and Orgogozo, L.: Numerical assessment of morphological and hydraulic properties of moss, lichen

628   and peat from a permafrost peatland, Hydrol. Earth Syst. Sci., 27, 431–451, doi:10.5194/hess-27-

629   431-2023, 2023.

630

631   De Vrese P., Georgievski G., Gonzalez Rouco J. F., Notz D., Stacke T., Steinert N. J., Wilkenskjeld

632   S., and Brovkin V.: Representation of soil hydrology in permafrost regions may explain large part

633   of inter-model spread in simulated Arctic and subarctic climate, The Cryosphere, 17, 2095–2118,

634   doi:10.5194/tc-17-2095-2023, 2023.

635

636   Domine F., Fourteau K., Picard G. *et al.*: Permafrost cooled in winter by thermal bridging through

637   snow-covered shrub branches. *Nat. Geosci.* **15**, 554–560, doi:10.1038/s41561-022-00979-2, 2022.

638

639   Duchkov AD, Sokolova LS, Balobaev VT, Devyatkin VN, Kononov VI, Lysak SV: Heat flow and

640   geothermal field in Siberia, Geologiya / Geofizika,38(11):1716-1729, 1997.

641

642   Essery R.: A factorial snowpack model (FSM 1.0), Geosci. Model Dev., 8, 3867–3876,

643   doi:10.5194/gmd-8-3867-2015, 2015.

644

645   Eyring V., Bony S., Meehl G. A., Senior C. A., Stevens B., Stouffer R. J., Taylor K. E.: Overview

646   of the Coupled Model Intercomparison Project Phase 6 (CMIP6) experimental design and

647   organization, Geosci. Model Dev., 9, 1937–1958, doi:10.5194/gmd-9-1937-2016, 2016.

648

649   Fan X., Duan Q., Shen C., Wu Y., Xing C.: Global surface air temperatures in CMIP6: historical

650   performance and future changes, Environ. Res. Lett. 15, 104056 , doi:10.1088/1748-9326/abb051,

651   2020.

652

653   Fedorov AN, Konstantinov PY, Vasilyev NF, Shestakova AA, The influence of boreal forest

654   dynamics on the current state of permafrost in Central Yakutia, Polar Science, Volume 22, 100483,

655   ISSN 1873-9652, doi:10.1016/j.polar.2019.100483, 2019.

656

31

657 Frolking S. : Sensitivity of spruce/moss boreal forest net ecosystem productivity to seasonal
658 anomalies in weather, Journal of Geophysical Research, 102(D24), 29053–29064,
659 doi:10.1029/96JD03707, 1997.

660

661 Gauthier S. et al., Boreal forest health and global change. Science 349, 819-822,
662 doi:10.1126/science.aaa9092, 2015.

663

664 Gentsch N. Permafrost soils in Central Siberia : landscape controls on soil organic carbon storage in
665 a light taiga biome. Munich, Germany: Akademische Verlagsgemeinschaft München; 2011.

666

667 Haesen S., Lembrechts J. J., De Frenne P., Lenoir J., Aalto J., Ashcroft M. B., Kopecký M., Luoto
668 M., Maclean I., Nijs I., Niittynen P., van den Hoogen J., Arriga N., Brůna J., Buchmann N., Čiliak
669 M., Collalti A., De Lombaerde E., Descombes P., … Van Meerbeek K: ForestTemp – Sub-canopy
670 microclimate temperatures of European forests. *Global Change Biology*, 27, 6307–6319,
671 doi:10.1111/gcb.15892, 2021.

672

673 Hamm A. and Frampton A.: Impact of lateral groundwater flow on hydrothermal conditions of the
674 active layer in a high-Arctic hillslope setting, The Cryosphere, 15, 4853–4871,
675 https://doi.org/10.5194/tc-15-4853-2021, 2021.

676

677 Hamon W.R.: Computation of direct runoff amounts from storm rainfall, International Association
678 of Scientific Hydrological Sciences Publication, 63:52-62, 1963.

679

680 Heijmans M.M.P.D., Magnússon, R.Í. Lara, M.J. *et al*: Tundra vegetation change and impacts on
681 permafrost. *Nat Rev Earth Environ* **3**, 68–84, doi:10.1038/s43017-021-00233-0, 2022

682

683 Hersbach H., Bell B., Berrisford P., Hirahara S., Horányi A., Muñoz-Sabater J., Nicolas J., Peubey
684 C., Radu R., Schepers D., Simmons A., Soci C., Abdalla S., Abellan X., Balsamo G., Bechtold P.,
685 Biavati G., Bidlot J., Bonavita M., De Chiara G., Dahlgren P., Dee D., Diamantakis M., Dragani R.,
686 Flemming J., Forbes R., Fuentes M., Geer A., Haimberger L., Healy S., Hogan R. J., Hólm E.,
687 Janisková M., Keeley S., Laloyaux P., Lopez P., Lupu C., Radnoti G., de Rosnay P., Rozum I.,
688 Vamborg F., Villaume S., Thépaut J.-N.: The ERA5 global reanalysis, Q. J. Roy. Meteor. Soc., 146,
689 1999–2049, doi:10.1002/qj.3803, 2020.

690

691 Hjort, J., Karjalainen, O., Aalto, J. *et al.*: Degrading permafrost puts Arctic infrastructure at risk by

692 mid-century. *Nat Commun* **9**, 5147, doi:10.1038/s41467-018-07557-4, 2018.

693

694 Hjort, J., Streletskiy, D., Doré, G. *et al.*: Impacts of permafrost degradation on infrastructure. *Nat*

695 *Rev Earth Environ* **3**, 24–38, doi:10.1038/s43017-021-00247-8, 2022.

696

697 Hock R.: Temperature index melt modelling in mountain areas, Journal of Hydrology, Volume 282,

698 Issues 1–4, Pages 104-115, doi:10.1016/S0022-1694(03)00257-9, 2003.

699

700 Holloway, JE, Lewkowicz, AG, Douglas, TA, et al. Impact of wildfire on permafrost landscapes: A

701 review of recent advances and future prospects. *Permafrost and Periglac Process*., 31, 371–382.

702 doi:10.1002/ppp.2048, 2020.

703

704 Hu G., Zhao L., Wu T., Wu X., Park H., Li R., et al.: Continued warming of the permafrost regions

705 over the Northern Hemisphere under future climate change. Earth's Future, 10, e2022EF002835,

706 doi:10.1029/2022EF002835, 2022.

707

708 Hu G., Zhao L, Li R., Park H., Wu X., Su Y., Guggenberger G., Wu T., Zou D., Zhu X., Zhang W.,

709 Wu Y., Hao J.: Water and heat coupling processes and its simulation in frozen soils: Current status

710 and future research directions, CATENA, Volume 222, 106844, ISSN 0341-8162,

711 doi:10.1016/j.catena.2022.106844, 2023.

712

713 Iturbide M., Fernández J., Gutiérrez J.M., Bedia J., Cimadevilla E., Díez-Sierra J., Manzanas R.,

714 Casanueva A., Baño-Medina J., Milovac J., Herrera S., Cofiño A.S., San Martín D., García-Díez

715 M., Hauser M., Huard D., Yelekci Ö.: Repository supporting the implementation of FAIR principles

716 in the IPCC-WG1 Atlas. Zenodo, doi: 10.5281/zenodo.3691645. Available from:

717 https://github.com/IPCC-WG1/Atlas, 2022.

718

719 Jan A. and Painter S.L.: Permafrost thermal conditions are sensitive to shifts in snow timing,

720 *Environ. Res. Lett.* **15** 084026, 2020.

721

722 Jan A.: Modeling the role of lateral surface flow in low-relief polygonal tundra. *Permafrost and*
723 *Periglac Process.*, 33(3): 214-225. doi:10.1002/ppp.2145, 2022.

724

725 Ji H., Nan Z., Hu J., Zhao Y. and Zhang Y.: On the spin-up strategy for spatial modeling of
726 permafrost dynamics: A case study on the Qinghai-Tibet Plateau. *Journal of Advances in Modeling*
727 *Earth Systems*, 14, e2021MS002750, doi:10.1029/2021MS002750, 2022.

728

729 Jin H., Huang Y., Bense V.F., Ma Q., Marchenko S.S., Shepelev V.V., Hu Y., Liang S., Spektor
730 V.V., Jin X. et al.: Permafrost Degradation and Its Hydrogeological Impacts. Water, 14, 372.
731 doi:10.3390/w14030372, 2022.

732

733 Karjalainen, O., Aalto, J., Luoto, M. *et al*: Circumpolar permafrost maps and geohazard indices for
734 near-future infrastructure risk assessments. *Sci Data* **6**, 190037, doi:10.1038/sdata.2019.37, 2019.

735 Karlsson J., Serikova S., Vorobyev S.N. *et al*: Carbon emission from Western Siberian inland
736 waters. *Nat Commun* **12**, 825, doi:10.1038/s41467-021-21054-1, 2021.

737

738 Kim J.-S. et al.: Extensive fires in southeastern Siberian permafrost linked to preceding Arctic
739 Oscillation, Sci. Adv.6,eaax3308, doi:10.1126/sciadv.aax3308, 2020.

740

741 Kirdyanov A.V., Saurer M., Siegwolf R., Knorre A.A, Prokushkin A.S., Churakova (Sidorova)
742 O.V, Fonti M.V., Büntgen U: Long-term ecological consequences of forest fires in the continuous
743 permafrost zone of Siberia, *Environ. Res. Lett.* **15** 034061, 2020.

744

745 Kirdyanov A.V., Saurer M., Arzac A., Knorre A.A., Prokushkin A.S., Churakova (Sidorova) O.V.,
746 Arosio T., Bebchuk T., Siegwolf R., Büntgen U.: Thawing permafrost can mitigate warming-
747 induced drought stress in boreal forest trees, Science of The Total Environment, Volume 912,
748 168858, ISSN 0048-9697, doi:10.1016/j.scitotenv.2023.168858, 2024.

749

750 Khani H.M., Kinnard C., Gascoin S., Lévesque E.: Fine-scale environment control on ground
751 surface temperature and thaw depth in a High Arctic tundra landscape. *Permafrost and Periglac*
752 *Process.* ; 34(4): 467-480. doi:10.1002/ppp.2203, 2023.

753

754   Kurylyk B.L., Watanabe K.! The mathematical representation of freezing and thawing processes in

755   variably-saturated, non-deformable soils, Advances in Water Resources, Volume 60, Pages 160-

756   177, ISSN 0309-1708, doi:10.1016/j.advwatres.2013.07.016., 2013.

757

758   Kurylyk, B.L.: Engineering challenges of warming, *Nat. Clim. Chang.* **9**, 807–808,

759   doi:10.1038/s41558-019-0612-8, 2019.

760

761   Lamontagne-Hallé P., McKenzie J.M., Kurylyk B.L., Zipper S.C. : Changing groundwater

762   discharge dynamics in permafrost regions, Environ. Res. Lett. 13 084017, 2018.

763

764   Li X.-Y., Jin H.-J., Wang H.-W, Marchenko S.S., Shan W., Luo D.-L., He R.-X., Spektor V.,

765   Huang Y.-D., Li X.-Y., Jia N., Influences of forest fires on the permafrost environment: A review,

766   Advances in Climate Change Research, Volume 12, Issue 1, 2021, Pages 48-65, ISSN 1674-9278,

767   doi:/10.1016/j.accre.2021.01.001, 2021.

768

769   Li G., Zhang M., Pei W., Melnikov A., Khristoforov I., Li R., Yu F., 2022a. Changes in permafrost

770   extent and active layer thickness in the Northern Hemisphere from 1969 to 2018, Science of The

771   Total Environment, Volume 804, 150182, ISSN 0048-9697, doi:10.1016/j.scitotenv.2021.150182,

772   2022.

773

774   Li C., Wei Y., Liu Y., Li L., Peng L., Chen J., et al.: Active layer thickness in the Northern

775   Hemisphere: Changes from 2000 to 2018 and future simulations. Journal of Geophysical Research:

776   Atmospheres, 127, e2022JD036785, doi:10.1029/2022JD036785, 2022b

777

778   Loranty M. M., Abbott B. W., Blok D., Douglas T. A., Epstein H. E., Forbes B. C., Jones B. M.,

779   Kholodov A. L., Kropp H., Malhotra A., Mamet S. D., Myers-Smith I. H., Natali S. M., O'Donnell

780   J. A., Phoenix G. K., Rocha A. V., Sonnentag O., Tape K. D. and Walker D. A.: Reviews and

781   syntheses: Changing ecosystem influences on soil thermal regimes in northern high-latitude

782   permafrost regions, Biogeosciences, 15, 5287–5313, doi:10.5194/bg-15-5287-2018, 2018.

783

784 Makarieva O., Nesterova N., Post D. A., Sherstyukov A. and Lebedeva L.: Warming temperatures
785 are impacting the hydrometeorological regime of Russian rivers in the zone of continuous
786 permafrost, The Cryosphere, 13, 1635–1659, doi:10.5194/tc-13-1635-2019, 2019.

787

788 Mashukov D.A., Benkova A.V., Benkova V.E. *et al.* Radial Growth and Anatomic Structure of the
789 Trunk Wood of Healthy and Stag-Headed Larch Trees on Permafrost. *Contemp. Probl. Ecol.* **14**,
790 767–774, doi:10.1134/S1995425521070143, 2021.

791

792 Miner K.R., Turetsky M.R., Malina E. *et al.* Permafrost carbon emissions in a changing Arctic. *Nat*
793 *Rev Earth Environ* **3**, 55–67. doi:10.1038/s43017-021-00230-3, 2022.

794

795 Nitzbon J., Krinner G., Schneider von Deimling T., Werner M., and Langer M.: First quantification
796 of the permafrost heat sink in the Earth's climate system. Geophysical Research Letters, 50,
797 e2022GL102053, doi:10.1029/2022GL102053, 2023.

798

799 Nitze I., Grosse G., Jones B.M. *et al:* Remote sensing quantifies widespread abundance of
800 permafrost region disturbances across the Arctic and Subarctic. *Nat Commun* **9**, 5423,
801 doi:10.1038/s41467-018-07663-3, 2018.

802

803 Obu J., Westermann S., Bartsch A., Berdnikov N., Christiansen H.H., Dashtseren A., Delaloye R.,
804 Elberling B., Etzelmüller B., Kholodov A., Khomutov A., Kääb A., Leibman M.O., Lewkowicz
805 A.G., Panda S.K., Romanovsky V., Way R.G., Westergaard-Nielsen A., Wu T., Yamkhin J., Zou
806 D., 2019. Northern Hemisphere permafrost map based on TTOP modelling for 2000–2016 at 1 km2
807 scale, Earth-Science Reviews, Volume 193, Pages 299-316, ISSN 0012-8252,
808 doi:10.1016/j.earscirev.2019.04.023, 2019

809

810 Obu J., Westermann S., Barboux C.; Bartsch A.; Delaloye R.; Grosse G.; Heim B.; Hugelius G.;
811 Irrgang A.; Kääb A.M.; Kroisleitner C.; Matthes H.; Nitze I.; Pellet C.; Seifert F.M.; Strozzi T.;
812 Wegmüller U.; Wieczorek M.; Wiesmann A.: ESA Permafrost Climate Change Initiative
813 (Permafrost_cci): Permafrost active layer thickness for the Northern Hemisphere, v3.0. NERC EDS
814 Centre for Environmental Data Analysis, 28 June 2021.
815 doi:10.5285/67a3f8c8dc914ef99f7f08eb0d997e23, 2021

816

817 Oehri J., Schaepman-Strub G., Kim JS. *et al.*: Vegetation type is an important predictor of the arctic

818 summer land surface energy budget. *Nat Commun* **13**, 6379, doi:10.1038/s41467-022-34049-3,

819 2022.

820

821 O'Neill B. C., Tebaldi C., van Vuuren D. P., Eyring V., Friedlingstein P., Hurtt G., Knutti R.,

822 Kriegler E., Lamarque J.-F., Lowe J., Meehl G. A., Moss R., Riahi, K., Sanderson B. M.: The

823 Scenario Model Intercomparison Project (ScenarioMIP) for CMIP6, Geosci. Model Dev., 9, 3461–

824 3482, doi:10.5194/gmd-9-3461-2016, 2016.

825

826 Orgogozo L., Prokushkin A.S., Pokrovsky O.S., Grenier C., Quintard M., Viers J., Audry S.: Water

827 and energy transfer modeling in a permafrost-dominated, forested catchment of Central Siberia: The

828 key role of rooting depth, Permafrost and Periglacial Processes, 30: 75–89 , doi:10.1002/ppp.1995 ,

829 2019.

830

831 Orgogozo L., Xavier T., Oulbani H., Grenier C.: Permafrost modelling with OpenFOAM®: New

832 advancements of the permaFoam solver, Computer Physics Communications, Vol. 282,

833 doi:10.1016/j.cpc.2022.108541, 2023.

834

835 Park SW., Kim JS. and Kug JS: The intensification of Arctic warming as a result of CO_2

836 physiological forcing. *Nat Commun* **11**, 2098, doi:10.1038/s41467-020-15924-3, 2020.

837

838 Park, SW., Kug, JS: A decline in atmospheric CO_2 levels under negative emissions may enhance

839 carbon retention in the terrestrial biosphere. *Commun Earth Environ* **3**, 289, doi:10.1038/s43247-

840 022-00621-4, 2022.

841

842 Pokrovsky O.S., Schott J.S., Kudryavtzev D.I., Dupré B.: Basalt weathering in Central Siberia

843 under permafrost conditions. Geochimica et Cosmochimica Acta, Vol. 69, No. 24, pp. 5659 –5680,

844 2005.

845

846 Prokushkin A., Kajimoto T., Prokushkin S., McDowell W., Abaimov A.P., Matsuura Y.: Climatic

847 factors influencing fluxes of dissolved organic carbon from the forest floor in a continuous-

848   permafrost Siberian watershed, Canadian Journal of Forest Research-Journal Canadien de la

849   Recherche Forestiere, 35, 2130-2140, doi:10.1139/x05-150, 2004.

850

851   Prokushkin A. S., Gleixner G., McDowell W. H., Ruehlow S. and Schulze, E.-D.: Source- and

852   substrate-specific export of dissolved organic matter from permafrost-dominated forested watershed

853   in central Siberia, *Global Biogeochem. Cycles*, 21, GB4003, doi:10.1029/2007GB002938, 2007.

854

855   Ramage J., Jungsberg L., Wang S. *et al.:* Population living on permafrost in the Arctic. *Popul*

856   *Environ* **43**, 22–38, doi:/10.1007/s11111-020-00370-6, 2021

857

858   Revich, B.A.; Eliseev, D.O.; Shaposhnikov, D.A. Risks for Public Health and Social Infrastructure

859   in Russian Arctic under Climate Change and Permafrost Degradation. *Atmosphere*, *13*, 532,

860   doi.org/10.3390/atmos13040532, 2022.

861

862   Rew L.J., McDougall K.L., Alexander J.M., Daehler C.C., Essl F., Haider S., Kueffer C., Lenoir J.,

863   Milbau A., Nuñez M.A., Pauchard A., Rabitsch W.: Moving up and over: redistribution of plants in

864   alpine, Arctic, and Antarctic ecosystems under global change, Arctic, Antarctic, and Alpine

865   Research, 52:1, 651-665, doi:10.1080/15230430.2020.1845919, 2020.

866

867   Schneider von Deimling, T., Lee, H., Ingeman-Nielsen, T., Westermann, S., Romanovsky, V.,

868   Lamoureux, S., Walker, D. A., Chadburn, S., Trochim, E., Cai, L., Nitzbon, J., Jacobi, S., and

869   Langer, M.: Consequences of permafrost degradation for Arctic infrastructure – bridging the model

870   gap between regional and engineering scales, The Cryosphere, 15, 2451–2471, doi:10.5194/tc-15-

871   2451-2021, 2021.

872

873   Schuur E.A.G. et al.: Permafrost and Climate Change: Carbon Cycle Feedbacks From the Warming

874   Arctic, Annual Review of Environment and Resources 2022 47:1, 343-371, 2022.

875

876   Shiklomanov N.I., Streletskiy D.A., Swales T.B., Kokorev V.A.: Climate Change and Stability of

877   Urban Infrastructure in Russian Permafrost Regions: Prognostic Assessment based on GCM

878   Climate Projections, Geographical Review, 107:1, 125-142, doi: 10.1111/gere.12214, 2017.

879

880   Sjöberg Y., Coon E., Sannel A. B. K., Pannetier R., Harp D., Frampton A., Painter S. L. and Lyon

881   S. W.: Thermal effects of groundwater flow through subarctic fens: A case study based on field

882   observations   and   numerical   modeling,   *Water   Resour.   Res.*,   52,   1591–1606,
883   doi:10.1002/2015WR017571, 2016.

885   Sonke J.E., Teisserenc R., Heimbürger-Boavida L.-E., Petrova M.V., Marusczak N., Le Dantec T.,
886   Chupakov A.V., Li C., Thackray C.P., Sunderland E.M., Tananaev N., Pokrovsky O.S.,: Eurasian
887   river spring flood observations support net Arctic Ocean mercury export to the atmosphere and
888   Atlantic   Ocean.   PNAS,   115,   50,   E11586–E11594,
889   www.pnas.org/cgi/doi/10.1073/pnas.1811957115, 2018.

891   Speetjens N. J., Hugelius G., Gumbricht T., Lantuit H., Berghuijs W. R., Pika P. A., Poste A. and
892   Vonk J. E.: The pan-Arctic catchment database (ARCADE) , Earth Syst. Sci. Data, 15, 541–554,
893   https://doi.org/10.5194/essd-15-541-2023, 2023.

895   Streletskiy D.A., Suter L.J., Shiklomanov N.I., Porfiriev B.N., Eliseev D.O.: Assessment of climate
896   change impacts on buildings, structures and infrastructure in the Russian regions on permafrost,
897   *Environ. Res. Lett.* **14** 025003, 2019.

899   Streletskiy D.A., Clemens S., Lanckman J.-P., Shiklomanov N.I.: The costs of Arctic infrastructure
900   damages   due   to   permafrost   degradation,   *Environ.   Res.   Lett.*   **18**   015006,
901   doi:10.1088/1748-9326/acab18, 2023.

903   Stuenzi S.M., Boike J., Gädeke A., Herzschuh U., Kruse S., Pestryakova L.A., Westermann S.,
904   Langer M.: Sensitivity of ecosystem-protected permafrost under changing boreal forest structures,
905   *Environ. Res. Lett.* **16** 084045, doi:10.1088/1748-9326/ac153d, 2021.

907   van Vuuren D. P., Edmonds J., Thomson A., Riahi K., Kainuma M., Matsui T., Hurtt G. C.,
908   Lamarque J.-F., Meinshausen M., Smith S., Granier C., Rose S. K., Hibbard K. A.: The
909   representative   concentration   pathways: an   overview.   Climatic   Change,   109,   5-31.
910   doi:10.1007/s10584-011-0148-z, 2011.

912   Viers J, Prokushkin AS, Pokrovsky OS, et al. Seasonal and spatial variability of elemental
913   concentrations in boreal forest larch foliage of Central Siberia on continuous permafrost.
914   Biogeochemistry, 113(1-3):435-449, doi:10.1007/s10533-012-9770-8, 2013.

916   Vitasse Y., Porté A.J., Kremer A. *et al.:* Responses of canopy duration to temperature changes in
917   four temperate tree species: relative contributions of spring and autumn leaf phenology. *Oecologia*
918   **161**, 187–198, doi:10.1007/s00442-009-1363-4, 2009.

919

920 Vitasse Y., François C., Delpierre N., Dufrêne E., Kremer A., Chuine I., Delzon S., 2011. Assessing

921 the effects of climate change on the phenology of European temperate trees, Agricultural and Forest

922 Meteorology, Volume 151, Issue 7, Pages 969-980, ISSN 0168-1923,

923 doi:10.1016/j.agrformet.2011.03.003, 2011.

924

925 Vonk J.E., Speetjens N.J. and Poste A.E.: Small watersheds may play a disproportionate role in

926 arctic land-ocean fluxes. *Nat Commun* **14**, 3442: doi:10.1038/s41467-023-39209-7, 2023.

927

928 Walvoord M.A. and Kurylyk B.L.: Hydrologic Impacts of Thawing Permafrost—A Review.

929 Vadose Zone Journal, 15: 1-20 vzj2016.01.0010, doi:10.2136/vzj2016.01.0010, 2016.

930

931 Walvoord M.A. and Striegl R.G.: Complex Vulnerabilities of the Water and Aquatic Carbon Cycles

932 to Permafrost Thaw. Front. Clim. 3:730402, doi: 10.3389/fclim.2021.730402, 2021.

933

934 Wang J. and Liu D.: Vegetation green-up date is more sensitive to permafrost degradation than

935 climate change in spring across the northern permafrost region. *Global Change Biology*, 28, 1569–

936 1582, https://doi.org/10.1111/gcb.16011, 2022.

937

938 Weller H.G., Tabor G., Jasak H., Fureby C.: A Tensorial Approach to Computational Continuum

939 Mechanics Using Object Orientated Techniques, Computers in Physics, 12, 620-631,

940 doi:10.1063/1.168744, 1998.

941

942 Wright S.N., Thompson L.M., Olefeldt D., Connon R.F., Carpino O.A., Beel C.R., Quinton W.L.,

943 Thaw-induced impacts on land and water in discontinuous permafrost: A review of the Taiga Plains

944 and Taiga Shield, northwestern Canada, Earth-Science Reviews, Volume 232, 104104, ISSN 0012-

945 8252, doi:10.1016/j.earscirev.2022.104104, 2022.

946

947 Zellweger F., Coomes D., Lenoir J. et al.: Seasonal drivers of understorey temperature buffering in

948 temperate deciduous forests across Europe. *Global Ecol Biogeogr*, 28: 1774–1786.

949 doi:10.1111/geb.12991, 2019.

950

951   Zellweger F. et al.: Forest microclimate dynamics drive plant responses to warming. Science 368,

952   772-775, doi:10.1126/science.aba6880, 2020.